

Radiation patterns in Figure 7(b) show that design B exhibits the low cross polarization level of -22 dB, conversely, design A and C has cross polarization level of -15 dB. In addition, design B has a wider symmetric radiation pattern than design A and C.

To understand the differences in the performance of the three designs, Figure 9 shows the electric field distribution at the aperture for all three designs. Ideally, the electric field distribution at the aperture of TSA should be purely horizontal to obtain best performance. Due to large metallic corrugation at the aperture, design A and C show impure electric field as marked in the circles. However, the knife edge corrugation for design B allows no degradation in the electric field which results in completely horizontal electric field distribution throughout the substrate. Therefore, in design B most of the field propagates in front direction and hence further improved side lobe levels in both E and H planes than uniform corrugated design which are further compared in Figure 8 based on CST simulator. This minimal degradation also results in superior cross polarization performance as compared to AFLTSA with uniform corrugation as shown in Figure 7(b). Superior performance of knife edge corrugation profile over uniform corrugation profile is also depicted in Figure 10.

5. CONCLUSION

This article has presented an improved wideband high gain AFLTSA with improved side lobe level. The proposed design, using a linearly decreasing depth of corrugation, has a wide impedance bandwidth, flat gain of 16 dB along with SLL of -18 and -14 dB in E and H plane, respectively. The structure exhibits a symmetric radiation pattern and low cross polarization level of -22 dB.

REFERENCES

1. T.S. Rappaport et al., Millimeter wave mobile communications for 5G cellular: It will work!, *IEEE Access* 1 (2013), 335–349.
2. S.N. Prasad and S. Mahapatra, A novel MIC slot-line antenna, In: 1979 9th European Microwave Conference, 1979, pp. 120–124.
3. S. Sugawara, Y. Maita, K. Adachi, K. Mori, and K. Mizuno, A mm-wave tapered slot antenna with improved radiation pattern, vol. 2, In: *Microwave Symposium Digest*, Denver, CO, 1997, pp. 959–962.
4. M. Sun, X. Qing, and Z.N. Chen, 60 GHz antipodal Fermi antenna on PCB, In: *Proceedings of the 5th European Conference on Antennas and Propagation (EUCAP)*, 2011, pp. 3109–3112.
5. Z. Briqech, A. Sebak, and T. Denidini, 60 GHz Fermi tapered slot antenna with sin-corrugation, In: *IEEE Antennas and Propagation Society International Symposium (APSURSI)*, Orlando, FL, 2013, pp. 160–161.
6. Z.-C. Hao, W. Hong, J. Chen, X.-P. Chen, and K. Wu, A novel feeding technique for antipodal linearly tapered slot antenna array, In: *2005 IEEE MTT-S International Microwave Symposium Digest*, Long Beach, CA, 2005.
7. F. Taringou, D. Dousset, J. Bornemann, and K. Wu, Broadband CPW feed for millimeter-wave SIW-based antipodal linearly tapered slot antennas, *IEEE Trans Antennas Propag* 61 (2013).
8. J.E. Rayas-Sanchez and V. Gutierrez-Ayala, A general EM-based design procedure for single-layer substrate integrated waveguide interconnects with microstrip transitions, In: *2008 IEEE MTT-S International Microwave Symposium Digest*, Atlanta, GA, 2008, pp. 983–986.
9. D.H. Schaubert, E.L. Kollberg, T. Korzeniowski, T. Thungren, J. Johansson, and K.S. Yngvesson, Endfire tapered slot antennas on dielectric substrates, *IEEE Trans Antennas Propag* 33 (1985), 1392–1400.

WIDE-FIELD CIRCULAR SAR IMAGING: AN EMPIRICAL ASSESSMENT OF LAYOVER EFFECTS

Sevket Demirci,¹ Enes Yigit,² and Caner Ozdemir¹

¹Department of Electrical-Electronics Engineering, Mersin University, Ciftlikkoy 33343, Mersin, Turkey; Corresponding author: sdemirci@mersin.edu.tr

²Vocational School of Technical Sciences, Mersin University, Ciftlikkoy 33343, Mersin, Turkey

Received 29 June 2014

ABSTRACT: In circular synthetic aperture radar (CSAR), targets are usually scanned over the complete azimuthal aperture of 360° . A major challenge inhibiting successful CSAR image production is encountered in two-dimensional imaging of relatively large scenes (i.e. wide-field scenarios). For such cases, the spatially variant radar signature gives rises to image degradations known as layover effects. In this paper, the imaging results for hypothetical and real complex targets using their CSAR data at C band are demonstrated to characterize these effects. In real experiments, a ground-based, outdoor CSAR system is exploited thanks to the circular balcony of a building that provides 270° view of targets. A spherical back-projection algorithm is used to focus near-field data and the reconstructed images are also cleaned out from clutter to more easily visualize the layover artifacts. © 2015 Wiley Periodicals, Inc. *Microwave Opt Technol Lett* 57:489–497, 2015; View this article online at wileyonlinelibrary.com. DOI 10.1002/mop.28884

Key words: circular synthetic aperture radar; layover; back-projection algorithm; clutter reduction; automatic target detection

1. INTRODUCTION

In circular synthetic aperture radar (SAR) (CSAR), an antenna at a fixed altitude moves along a circular path while illuminating the interior ground region of the scanning path. This kind of collection geometry provides very high resolution imagery as a consequence of observation of targets over the complete aperture of 360° [1–3]. Additionally, CSAR systems have also three-dimensional (3D) resolution capability meaning that the height information can be readily attained even from a single-pass data [4]. Due to these unique properties, CSAR has been widely used in various tasks, such as; geosynchronous CSAR imaging [5], high resolution mapping of urban areas [6], automatic target recognition (ATR) of vehicles [7–13] and so forth.

Although CSAR offers important advantages over linear SAR, there are also serious challenges. In particular, the two-dimensional (2D) CSAR images of wide-field collections are generally exposed to image artifacts related to layover phenomenon [1,12]. Wide-field refers to CSAR geometries wherein the size of the scene is not much smaller than the scanning radius [8]. Together with wide azimuthal viewing, this geometry dictates that the backscattered signals of distinct scatterers superpose in the same range-azimuth cell. This phenomenon termed as layover causes the target's radar signature to vary spatially, which means that the same target can be shown quite different when imaged at different orientations and translations. Hence, for an accurate identification of targets especially in ATR missions, it is important to know how layover behaves as a function of radar parameters, data collection geometry and different target positions.

From the theoretical view, impulse-response (IPR) functions can be used to characterize layover aliasing. However, for a point scatterer displaced from the imaging center, it is known to be difficult to obtain a closed-form IPR solution [2]. For this

TABLE 1 CSAR System Parameters used in Simulation and Real Experiments

Parameter	Value
Scanning radius R_g (m)	21.9
Height of the antenna Z_c (m) and Corresponding depression angle θ ($^\circ$) w.r.t. origin	9.54, 23.5 10.64, 25.9
Frequency range, (GHz)	21.9, 45
Frequency sampling interval (MHz)	4.5 ~ 6
Azimuth angle sampling interval $\Delta\phi$ ($^\circ$)	3.75
	0.25
	0.5
Max. detection range from the antenna (m)	39.9

that are proportional to the heights of the scatterers. To be more specific, the reflection received at a particular viewpoint and from a single point at r_1 range will be displaced in the image by an amount of $(r_0 - r_1)$, where r_0 is the distance from radar to the imaging center. The value of this displacement will not be changed during the views of other look angles as the point lies on the center and scanning route has a circular trajectory. Thus, the response will be shown up as a defocusing circle. Second, the imaging of an off-centered target denoted by T2 can be considered. Considering a single scatterer at the range of r_{11} , the value of the displacement will now be changed as a function of the antenna position. Consequently, defocusing or layover effects will be resulted as an ellipse since the difference between r_{20} and r_{21} is bigger than that of r_{10} and r_{11} .

3. IMAGING RESULTS

Various simulation and real experiments were conducted to characterize layover effects in 2D CSAR imaging. Throughout the study, stepped frequency radar operation was adopted and data were acquired for the parameter values given in Table 1. The BP algorithm modified to near-field CSAR geometries [16] was used in all image reconstruction tasks.

3.1. Simulation Results

As explained in Subsection 2.2., layover distortions highly depend on the geometrical relationship between the radar and the scene. To investigate these dependencies, three different imaging simulations were performed for various combinations of data collection parameters, target positions and imaging (focal) planes.

In the first simulation, layover effects were analyzed by varying the relative distances between the target's position, the imaging center and the imaging plane. For this purpose, a point scatterer located at changing coordinates of 3D space was imaged onto two different focal planes of z_f . The values of the depression angle and the angular step were adjusted to be $\theta = 23.5^\circ$ and $\Delta\phi = 0.25^\circ$, respectively. Figure 3 shows the results for three different cases where the target is on-center, offset by 7.5 m only along x -direction and offset by 7.5 m in both x and y directions. Ground-plane results are shown in Figure 3(a) whereas the results for $z_f = 4\text{m}$ above the ground are shown in Figure 3(b). First, the effect of changing the relative distance between the target height and the imaging plane can be investigated by comparing the images on the same columns. As expected, the response is focused when the target height z_t is equal to the height of the imaging plane z_f [see Figure 3(a)];

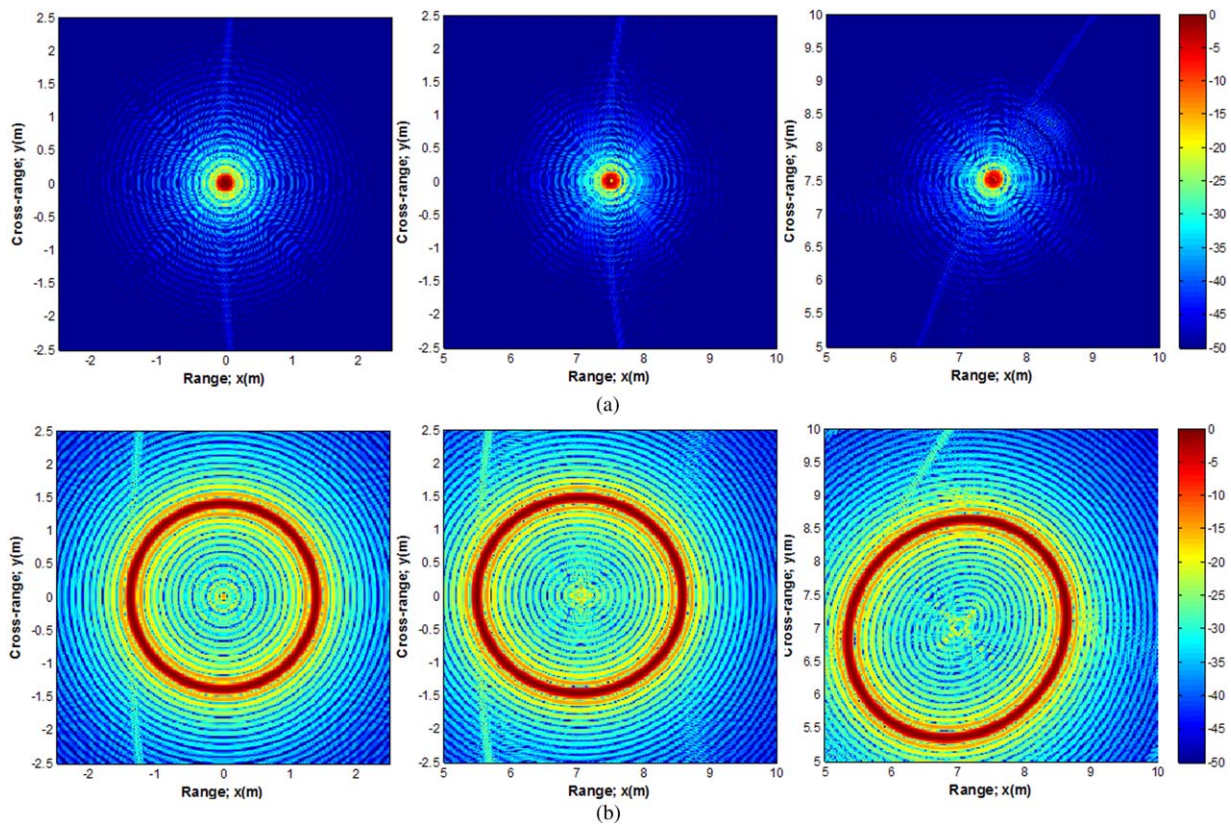


Figure 3 Imaging results ($\Delta\phi = 0.25^\circ$ case) for a point scatterer located at different positions and for different imaging planes z_f . (a) $z_f = 0$, (b) $z_f = 4$ m above the ground (Left: point is at the coordinate center, Middle: point is off-centered 7.5 m along x -direction, Right: point is off-centered 7.5 m in both x and y directions). [Color figure can be viewed in the online issue, which is available at wileyonlinelibrary.com]

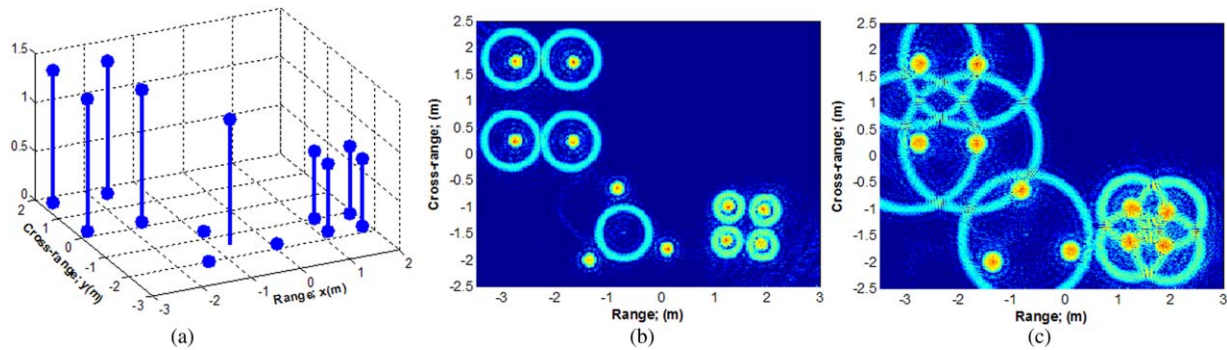


Figure 4 Illustration of the layover artifacts due to depression angle. (a) Multiple point targets in 3D space. Ground plane imaging results for (b) $\theta = 23.5^\circ$ and (c) $\theta = 45^\circ$. [Color figure can be viewed in the online issue, which is available at wileyonlinelibrary.com]

otherwise it is shown up as a defocusing ring [see Figure 3(b)]. Second, the effect of varying the offset distance between a particular point and the imaging center can be assessed by interpreting the images on the same rows. It is observed that when the image is focused, the displacement has almost no adverse effect; otherwise the original circular shape of the defocusing ring turns into an ellipse. Additionally, noting the (x, y) coordinates of the offset points which are $(7.5 \text{ m}, 0)$ and $(7.5 \text{ m}, 7.5 \text{ m})$, the resulted ellipse is also shown to be asymmetric with respect to these target coordinates.

In the second simulation, the dependency of layover artifacts on depression angle was investigated. For this purpose, a scene consisting of 20 point scatterers was selected [see Figure 4(a)] and data were gathered for two different values of depression angle, $\theta = 23.5^\circ$ and $\theta = 45^\circ$. The ground plane imaging results are shown in Figures 4(b) and 4(c). The obtained images reveal that the radii of the defocusing rings for the $\theta = 45^\circ$ case are larger than those of the $\theta = 23.5^\circ$ case. It can be also distinguished that the resolution gets worse as the depression angle value increases.

In the last simulation, aliasing effects were investigated for targets that involve linear structures. A total of 400 uniformly spaced point scatterers were placed between $x = -2 \text{ m}$ and 2 m of the 3D space as shown in Figure 5(a). The backscattering data were acquired for $\theta = 23.5^\circ$ and $\Delta\phi = 0.25^\circ$. As shown in Figure 5(b), the simulated image has four symmetric aliasing patterns. Hence, we can deduce that the CSAR imagery of closely spaced scatterers with a linear structure is exposed to aliasing patterns such as shown in Figure 5(b). As, CSAR is often used to obtain the radar images of military and civilian

vehicles that contain flat components; this phenomenon is possibly expected to be observed in the measured images of such targets. The experimental results that validate this finding will be demonstrated in Subsection 3.2.

3.2. Experimental Results

The characteristics of wide-field CSAR were experimentally investigated by utilizing the parameter values given in Table 1. A circular-shaped balcony platform was exploited to collect single-pass CSAR data. The photograph of the platform and the schematic diagram of its experimental usage are shown in Figures 6(a) and 6(b), respectively. The balcony has a height of $Z_c = 9.54 \text{ m}$ from the ground surface and a rotational structure that allows up to 270° azimuthal viewing with a scanning radius of $R_g = 21.9 \text{ m}$. This deployed geometry results in a wide-field application for most target sizes such that an 4 m radius of target enclosing circle corresponds to the 18.2% fraction of this scanning path's radius. The value for the angular sample spacing $\Delta\phi$ was set to 0.25° . The quasimonostatic operation was adopted and the horn antennas arranged in HH polarization geometry were located onto a wheel platform in order to manually move them on the synthetic aperture. The stepped frequency waveforms were generated by the help of a handheld vector network analyzer (VNA) with a model number of Anritsu MS2026C. The IF bandwidth of the VNA was adjusted to a low value, that is, 1 kHz to transmit more power.

3.2.1. Imaging of a Quad-trihedral and a Sphere Target.

In the first experiment, a quad-trihedral (QT) with side lengths of

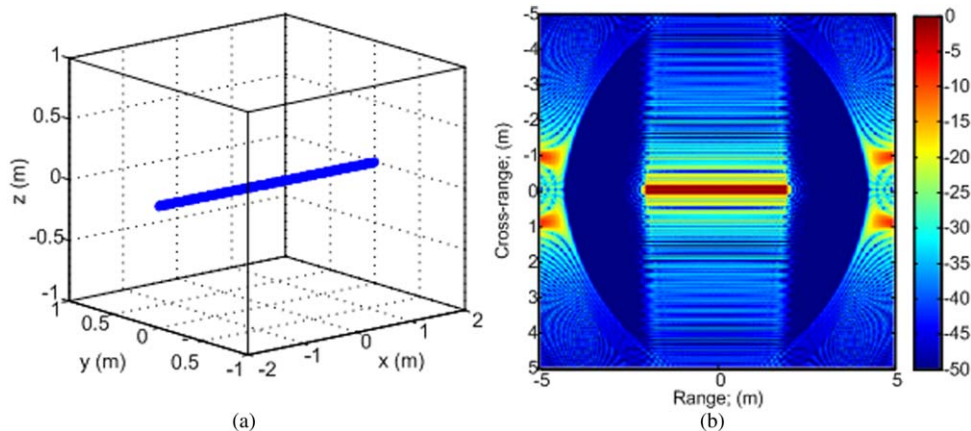


Figure 5 Aliasing effects in CSAR imaging of linearly shaped targets. (a) Target model constructed with point scatterers. (b) Ground plane imaging result. [Color figure can be viewed in the online issue, which is available at wileyonlinelibrary.com]



Figure 6 CSAR measurement facility, (a) photograph of the building with a circular structure, (b) schematic diagram for the structure's experimental usage. [Color figure can be viewed in the online issue, which is available at wileyonlinelibrary.com]

10 cm and a big sphere with a diameter of 50 cm were selected as targets. A QT is a reflector composed of four trihedral corner reflectors placed adjacently. With this geometry, a QT is able to exhibit strong returns from any azimuth. As seen in the photograph of Figure 7(a), the sphere was located at a height of 1.3 m and the QT was placed onto the ground. The depression angle value was set to $\theta = 23.5^\circ$. Figures 7(b) and 7(c) shows the ground-plane images while Figure 7(d) shows the reconstruction onto $z_f = 1.3$ m plane. As expected, the QT represents quite high reflections due to its corner structure. However, its response is deviated from ideal point scattering even in the ground plane image wherein the relative height is zero. This can be attributed to the three times bounce of the incident waves by the faces of each trihedral. Conversely, the layover effect can be easily discerned from the wider response of QT as seen in Figure 7(d). It is seen that as the difference between the imaging plane and target's vertical position increases, the response tends to become wider.

3.2.2. Imaging of a Car Sedan. In the second experiment, a car sedan (Scoda Octavia model) was scanned with $\theta = 23.5^\circ$ and for two different target positions; that is, target is on-center and target is off-centered by 7 m in y -direction. The upper images in Figure 8 show the photographs of these scenes. The car has dimensions of $(4.56L \times 1.77W \times 1.46H)$ m causing a near-field illumination under a LOS distance of 23.8 m. The ground plane imaging results for the on-center target are shown in the middle and bottom images of Figure 8(a). The middle image provides a wide view reconstruction while the bottom one gives a close up view of the target. It is seen that the car's shape is almost outlined together with nearly accurate length ($L_{\text{meas}} = 4.40$ m) and width $W_{\text{meas}} = 1.64$ m) extents. The strong reflections are seemed to be concentrated on the sides of the car. This can be explained by the multipath bounce between the car's lateral side and the ground plane which produces a high reflection mechanism. This phenomenon is less observed for the

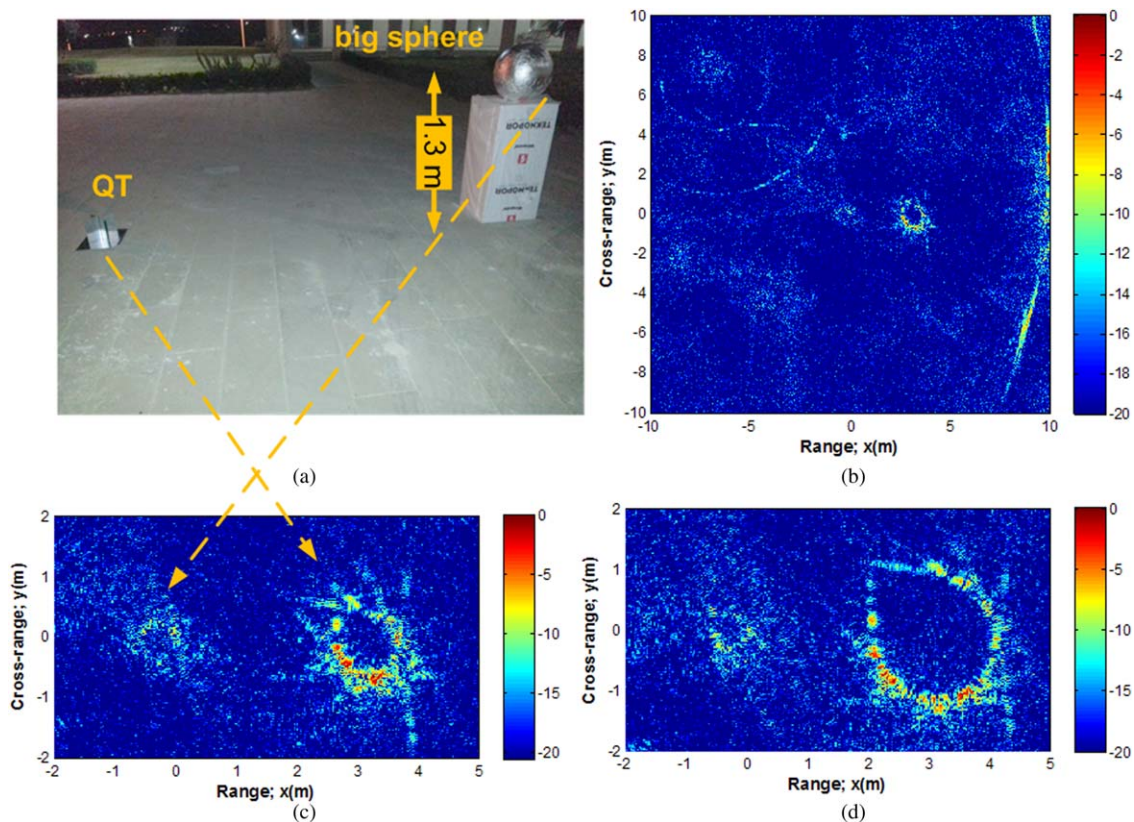


Figure 7 Results for the first experiment. (a) Targets' photograph. CSAR images for (b) wide-view, $z_f = 0$ plane (c) close-up view, $z_f = 0$ plane (d) close-up view, $z_f = 1.3$ m plane. [Color figure can be viewed in the online issue, which is available at wileyonlinelibrary.com]

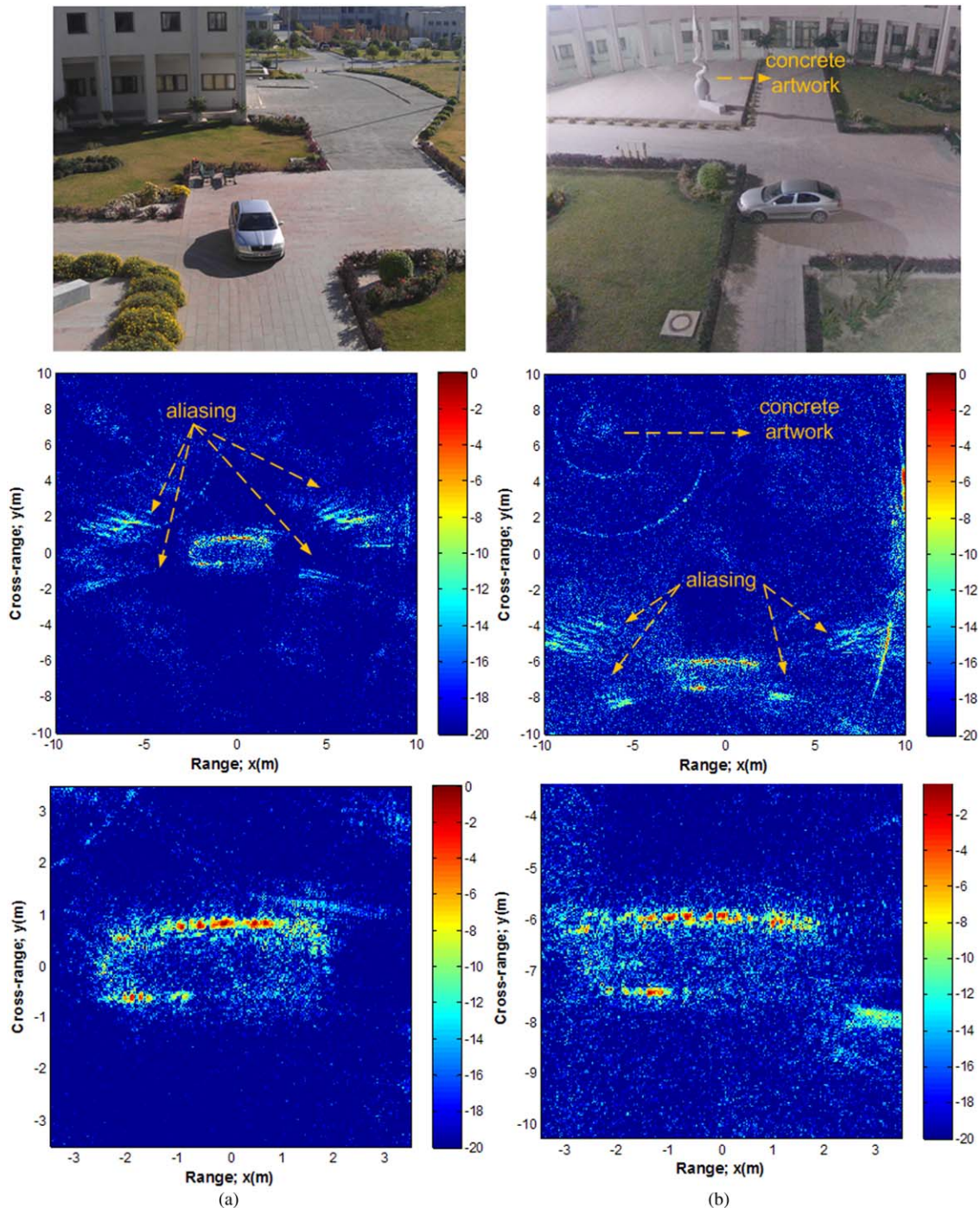


Figure 8 Results for the second experiment. The car is (a) on-center (b) off-centered 7 m along y-direction (Top: Target photographs, Middle: wide-view image, Bottom: close-up view image. [Color figure can be viewed in the online issue, which is available at wileyonlinelibrary.com]

front and back regions of the vehicle since these have smaller heights and also have less sharp parts. As expected, the car's left-rear is also shown to have weaker scattering since this region was not encompassed within the look angle of 270° aperture. Subsequently, the effects of an off-centered target can be evaluated by interpreting the images given in Figure 8(b). The addition of an offset produces little variations in the overall shape of the car's radar signature. However, there is a notable increase in the measured length ($L_{\text{meas}} = 4.69$ m). This is due to the fact that the vehicle's longitudinal parts especially the front and back edges are exposed to high layover since they have larger offset distances.

It is seen from the wide view images that there are also other strong reflection mechanisms. First, a concrete artwork within the scene manifests itself as nested rings at the upper left of the images. The centers of these rings, all being the same, also match with the actual coordinates of the artwork. These defocusing rings, as explained in Subsection 3.1., are due to the difference between the imaging plane and the heights of the scattering centers on this tall target. Second, the reflections seen symmetrically at the diagonals of the car resemble the aliasing effects relating to linear structures (see Fig. 5). The existence of these signatures in both images of on-center and off-centered target points out that these patterns should be associated with the aliasing effects due to linear structures.

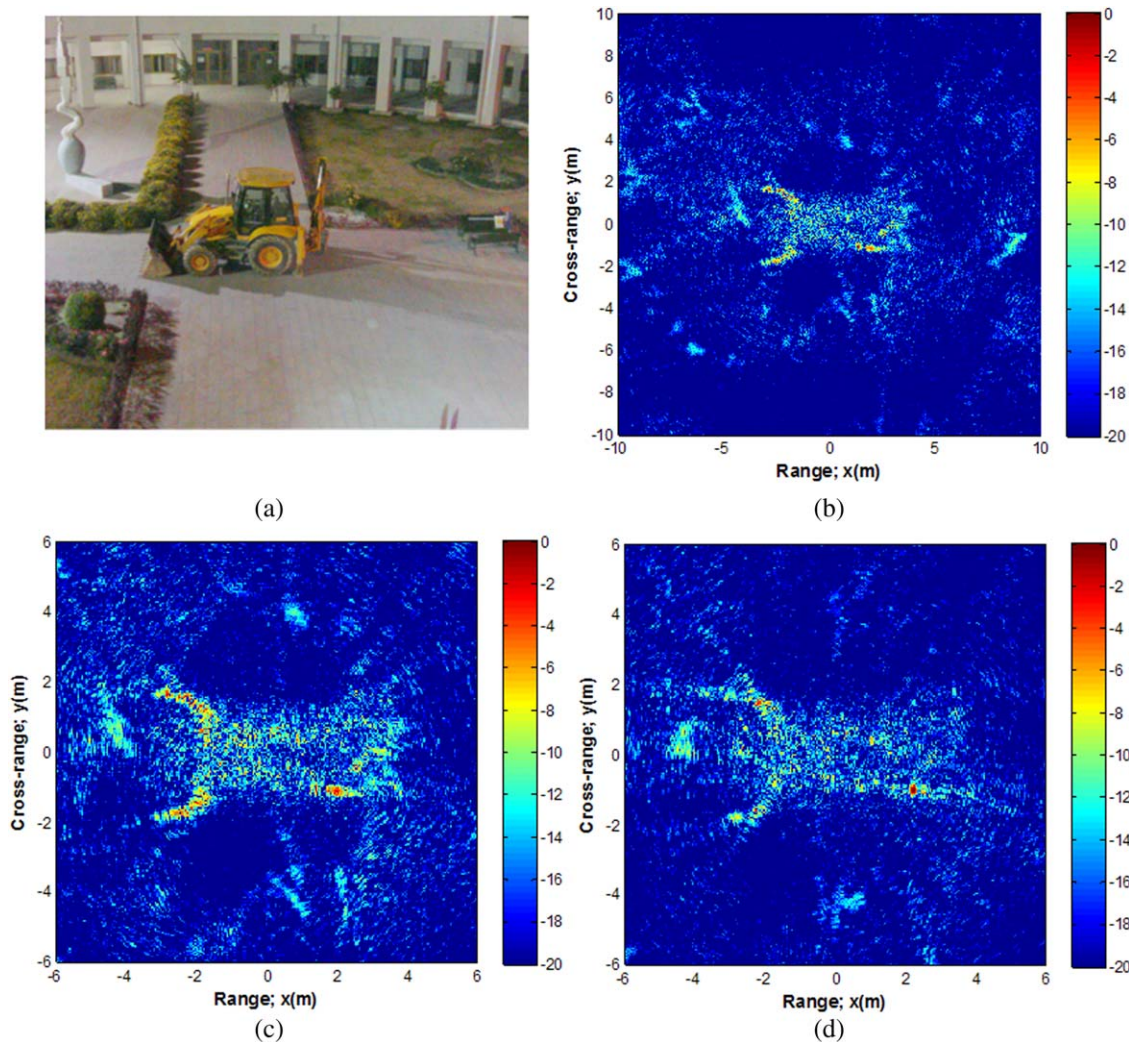


Figure 9 Results for the third experiment. (a) Target photograph. CSAR images for (b) wide-view, $\theta = 23.5^\circ$ (c) close-up view, $\theta = 23.5^\circ$ (d) close-up view, $\theta = 25.9^\circ$. [Color figure can be viewed in the online issue, which is available at wileyonlinelibrary.com]

3.2.3. Imaging of a Backhoe. In the third experiment, a loader backhoe (JCB 3CX) was tried as a more complex target. The photograph of the vehicle is shown in Figure 9(a). With this pose, the backhoe has dimensions of $(7.49L \times 2.4W \times 2.87H$ m) whose length size (i.e., maximum extent) corresponds to a

34% fraction of the scanning path's radius. Hence, a more wider-field application was realized when compared to the previous experiment. Two different elevation measurements were performed by setting $\theta = 23.5^\circ$ and $\theta = 25.9^\circ$. Ground-plane imaging results for the $\theta = 23.5^\circ$ case are shown in Figure 9(b)

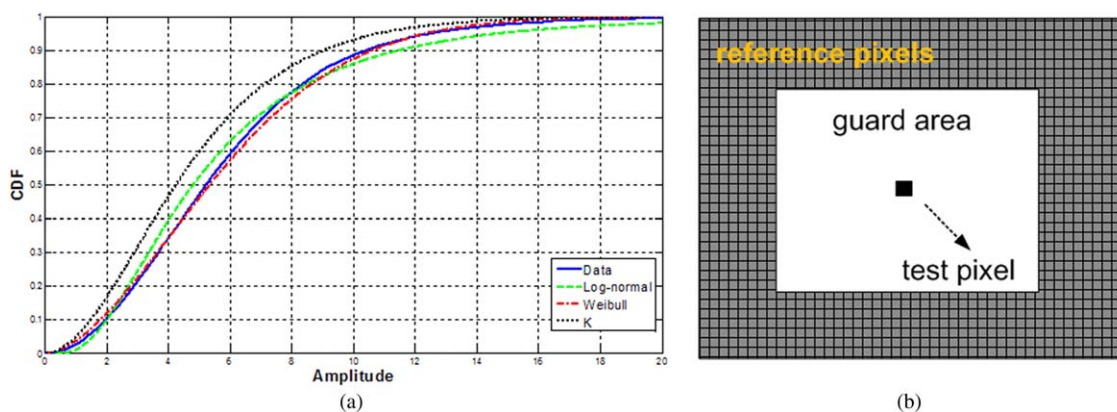


Figure 10 Clutter recognition and removal. (a) Theoretical CDFs of the fitted distributions and the empirical CDF of the sample clutter data. (b) Sliding window setup used in determination of the adaptive threshold value of the CFAR detector. [Color figure can be viewed in the online issue, which is available at wileyonlinelibrary.com]

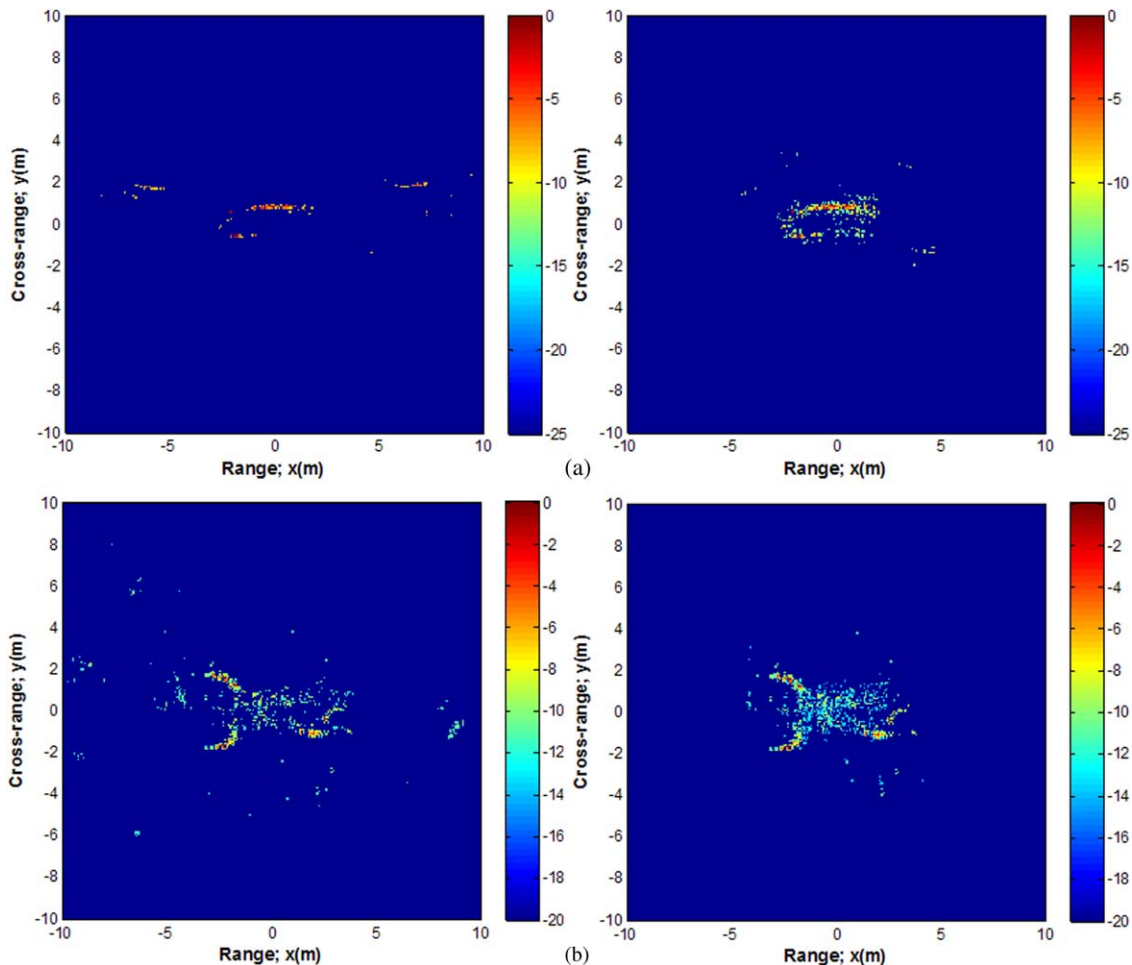


Figure 11 Clutter removal results for (a) the Car Sedan, (b) the Backhoe ($\theta = 23.5^\circ$) targets. (Left: Fixed thresholding, Right: CFAR detector ($P_{fa} = 0.01$) outputs. [Color figure can be viewed in the online issue, which is available at wileyonlinelibrary.com]

as a wide-view and in Figure 9(c) as a close-up view. The overall length and width of the vehicle is shown to be consistent with its true dimensions. In addition, the loader section can also be easily discerned from the U-shaped reflection pattern. This is due to the loader's low height in the current pose and as well as its strong corner-type reflection mechanism. The other parts such as cabin, however, are poorly focused since these highly elevated parts are severely exposed to layover. Conversely, the image for the $\theta = 25.9^\circ$ case demonstrates the notably changing signature for a slightly increased depression angle, as shown in Figure 9(d). This proves experimentally that the increase in the depression angle value causes more degradation in imaging quality.

4. CFAR DETECTION RESULTS

The obtained CSAR images are shown to have quite heavy clutter signals that interfere with targets. Thus, it becomes somewhat difficult to infer whether an investigated signature around the target is belonging to the target or background. This judgment may be beneficial in determination of the target's lay-over points which in turn may facilitate layover inversion task generally employed in 3D imaging purposes. The most straightforward way to eliminate clutter in SAR images is to apply a non-adaptive global threshold which may be termed as the fixed thresholding. However, this method results in either target signature loss or significant clutter energies when the signal-to-clutter

ratio (SCR) is large. Therefore, it is necessary to employ adaptive thresholding schemes for an improved detection.

In this work, a CFAR detector (see [17] for details) was used as being the most commonly used adaptive thresholding routine. For this purpose, clutter recognition was performed first. The magnitude data of the target-free regions were analyzed to find the best statistical distribution to model these clutter data. The popular models to characterize the clutter statistics, namely; Log-normal, Weibull and K-distribution were selected and their parameters for the best fit were obtained through a maximum likelihood estimation procedure. With the estimated parameters, the cumulative density functions (CDFs) were calculated and compared to the empirical CDF of the sample clutter data. The results are shown in Figure 10(a) which demonstrate that the Weibull CDF follows the empirical CDF more closely than the others. Next, a CFAR detector based on this Weibull clutter model [17] was applied to the amplitude data of attained images. As shown from Figure 10(b) a sliding window was used to compare the signal magnitudes at each pixel to an adaptive threshold value computed from a weighted combination of the signals from a window of reference pixels. More clearly, at each step, the parameters of the Weibull distribution were estimated by using the background samples of this window. Then, the threshold for the desired value of the probability of false alarm (P_{fa}) was computed by using this model and finally used in the hypothesis test.

The clutter removal results for the "Car Sedan" and the "Backhoe ($\theta = 23.5^\circ$)" targets are shown in Figures 11(a) and

11(b), respectively. It is seen that the conventional fixed thresholding approach is not able to detect weak target responses thereby causing much loss of the target features. This is due to high SCR values of the original CSAR images of these targets. Conversely, CFAR detection is seen to be capable of discriminating even the very weak signatures of targets demonstrating its success under more complex target situations.

5. CONCLUSION

In this work, the 2D imaging characteristics of wide-field CSAR geometries have been investigated. The layover effects were first analyzed and reviewed by forming the point response images for a changing relationship between the position of the off-center target and the height of the imaging plane. It was observed that, the ring-shaped defocusing signatures may dominate the imagery especially for the higher values of the depression angle and the larger offset distances. Then, the ground-based 270° aperture, CSAR experiments were performed to experimentally evaluate these adverse effects. The imaging results of both canonical and complex targets were seen to have scattering features that obey the facts obtained in the simulated examples. The dependency of the imaging quality on the depression angle and the extents of the target were all validated through the measured images of these targets. A clutter reduction algorithm was also exploited and applied to the CSAR images to facilitate the extraction of the target's scattering centers. The target-only images were successfully generated which can be analyzed in a further study, to invert layover and thereby obtain 3D information about the target.

ACKNOWLEDGMENT

The authors wish to acknowledge Mr. Hakan Istiker for his contributions to the experimental study.

REFERENCES

- C.V. Jakowatz, Jr., D.E. Wahl, P.H. Eichel, D.C. Ghiglia, and P.A. Thompson, Spotlight-mode synthetic aperture radar: A signal processing approach, Kluwer Academic Publishers, Norwell, MA, 1996.
- M. Soumekh, Synthetic aperture radar signal processing, Wiley, New York, 1999.
- C. Ozdemir, Inverse synthetic aperture radar imaging with MATLAB algorithms, Chapt 4, Wiley, Hoboken, NJ, 2012.
- L.J. Moore and L.C. Potter, Three-dimensional resolution for circular synthetic aperture radar, Proc SPIE 6568, E. G. Zelnio and F. D. Garber, eds., April 2007.
- Q. Liu, W. Hong, W.X. Tan, Y. Lin, Y.P. Wang, and Y.R. Wu, An improved polar format algorithm with performance analysis for geosynchronous circular SAR 2D imaging, Prog Electromagn Res (PIER) 119 (2011), 155–170.
- H.M. J. Cantaloube, E. Colin-Koeniguer, and H. Oriot, High resolution SAR imaging along circular trajectories, In: IEEE International Geoscience and Remote Sensing Symposium, 2007.
- M.L. Bryant, L.L. Gostin, and M. Soumekh, 3-D E-CSAR imaging of a T-72 tank and synthesis of its SAR reconstructions, IEEE Trans Aero Electron Sys 39 (2003), 211–227.
- K.E. Dungan and L.C. Potter, Classifying civilian vehicles using a wide-field circular SAR, In: Algorithms for Synthetic Aperture Radar Imagery XVI, Proc. SPIE, E. G. Zelnio and F. D. Garber, Eds., Vol. 7337 (2009).
- K. E. Dungan, C. Austin, J. Nehrbass, and L.C. Potter, Civilian vehicle radar data domes, In: Proc. SPIE 7699, Algorithms for Synthetic Aperture Radar Imagery XVII (2010), 76990P; Doi:10.1117/12.850151.
- L. Yu and Y. Zhang, A 3D target imaging algorithm based on two-pass circular SAR observations, Prog Electromagn Res (PIER) 122 (2012), 341–360.
- E. Ertin, C.D. Austin, S. Sharma, R.L. Moses: L.C. Potter E.G. Zelnio, and F.D. Garber, GOTCHA experience report: Three-dimensional SAR imaging with complete circular apertures, In: Proc. Algorithms for Synthetic Aperture Radar Imagery XIV, SPIE Defense and Security Symp., (2007).
- K. E. Dungan and L. C. Potter, 3-D Imaging of vehicles using wide aperture radar, IEEE Trans Aero Electron Syst 47 (2011).
- C.H. Casteel, Jr., L.A. Gorham, M.J. Minardi, S.M. Scarborough, K. D. Naidu, and U.K. Majumder, A challenge problem for 2D/3D imaging of targets from a volumetric data set in an urban environment, In: Algorithms for Synthetic Aperture Radar Imagery XIV, ser. Proc. SPIE, E. G. Zelnio and F. D. Garber, Eds., Vol. 6568, p. 65680D, 2007.
- D.C. Munson, J.D. O'Brien, and W.K. Jenkins, A tomographic formulation of spotlight-mode synthetic aperture radar, Proc IEEE 71 (1983), 917–925.
- J.L. Bauck and W.K. Jenkins, Tomographic processing of spotlight mode synthetic aperture radar signals with compensation for wavefront curvature, In: International Conference on Acoustics, Speech, and Signal Processing, ICASSP-88, Vol. 2, (1988), pp. 1192–1195.
- S. Demirci, H. Cetinkaya, E. Yigit, C. Ozdemir, and A. Vertiy, A study on millimeter-wave imaging of concealed objects: Application using back-projection algorithm, Prog Electromagn Res (PIER) 128 (2012), 457–477.
- S. Demirci, C. Ozdemir, A. Akdagli and E. Yigit, Clutter reduction in synthetic aperture radar images with statistical modeling: an application to MSTAR data, Microwave Opt Technol Lett 50 (2008), 1514–1520.

© 2015 Wiley Periodicals, Inc.

RECONFIGURABLE NOTCHED WIDEBAND ANTENNA USING EBG STRUCTURE

Huda A. Majid, Mohamad Kamal, A. Rahim, Mohamad R. Hamid, Norasniza A. Murad, Nor Asmawati Samsuri, Mohd Fairus Mohd Yusof, and Osman Ayop

UTM-MIMOS Center of Excellence, Communication Engineering Department, Faculty of Electrical Engineering, Universiti Teknologi Malaysia, 81310 UTM JB, Johor, Malaysia; Corresponding author: mkamal@fke.utm.my

Received 29 June 2014

ABSTRACT: In this article, a wideband monopole antenna with band notched reconfigurability is proposed. The antenna consists of a wideband monopole antenna, incorporated with reconfigurable electromagnetic bandgap (EBG) structures. Six EBG structures with different band notched frequency are used to achieve six band notched reconfigurations. The EBG structures are placed underneath the feed line of the antenna. A switch is placed at each EBG structure, and by controlling the state of the switch, the band notched operation of the EBG can be activated or deactivated. The proposed antenna is capable to provide useful features for the notched band UWB communication system. © 2015 Wiley Periodicals, Inc. Microwave Opt Technol Lett 57:497–501, 2015; View this article online at wileyonlinelibrary.com. DOI 10.1002/mop.28882

Key words: wideband antenna; electromagnetic bandgap; reconfigurable notched antenna

1. INTRODUCTION

In recent years, wideband communication systems are rapidly growing and attracted a lot of attention. The existing wireless communication systems such as WLAN 802.11 a/b/g/n, WiMAX 802.16, and C band satellite communication, however, interferences with the wideband operating system. To avoid the